Research Square

Preprints are preliminary reports that have not undergone peer review.
They should not be considered conclusive, used to inform clinical practice,
or referenced by the media as validated information.

Carbon partitioning through the pentose phosphate pathway regulates behavioral maturation in honeybees via a redox–endocrine axis

YUEHLUNG WU

runwu@ntu.edu.tw

National Taiwan University

Yun-Heng Lu

National Taiwan University, Department of Entomology

Yao-Kuang Tseng

National Taiwan University, Department of Entomology

Wei-Chan Chang

National Taiwan University, Department of Entomology

Article

Keywords: Apis mellifera, Deformed Wing Virus, Oxidative pentose phosphate pathway, Juvenile hormone, Division of labor, Carbon partitioning

Posted Date: July 21st, 2026

DOI: https://doi.org/10.21203/rs.3.rs-10237133/v1

License: This work is licensed under a Creative Commons Attribution 4.0 International License.
Read Full License

Additional Declarations: There is **NO** Competing Interest.

Abstract

Metabolic reprogramming is a hallmark of host–pathogen interactions, yet how infection-induced metabolic changes are translated into endocrine and behavioral outcomes remains poorly understood. Here, we identify a metabolic–endocrine axis linking pathogen-induced carbon reallocation to behavioral perturbation in the western honey bee. Using ^{13}C stable isotope tracing and flux-resolved metabolomics, we show that deformed wing virus infection redistributes glucose-derived carbon from ATP-generating pathways toward the high-turnover oxidative pentose phosphate pathway (oxPPP). We further show that oxPPP-derived NADPH supports juvenile hormone (JH) biosynthesis by providing reducing equivalents for the cytochrome P450-dependent terminal epoxidation catalyzed by methyl farnesoate epoxidase (MFE). Functional perturbation experiments show that oxPPP inhibition suppresses JH elevation and delays precocious behavioral maturation, indicating a critical role of the oxPPP in coupling endocrine activation to behavioral outcomes. Thermal and chemical stressors similarly increase G6PD activity and NADPH production, suggesting that the oxPPP–NADPH axis represents a conserved metabolic hub integrating diverse environmental challenges. Together, our findings identify carbon partitioning as a functional regulator of endocrine-associated behavioral maturation and reveal a metabolic–redox–endocrine axis through which stress-induced metabolic remodeling can influence behavior. This framework provides an invertebrate model for understanding how stress-responsive carbon partitioning may regulate NADPH-dependent endocrine systems across both invertebrate and vertebrate contexts.

Introduction

Organisms must dynamically reallocate metabolic resources to navigate changing environments. Yet how stress-induced intracellular metabolic flux changes are translated into systemic endocrine and behavioral phenotypes remains a fundamental unresolved question in physiology. It is well established that cell-intrinsic metabolic reprogramming, such as the shifts in glycolysis, mitochondrial activity, and lipid metabolism, is a hallmark of stress and immune responses [1-5]. Crucially, metabolic intermediates are increasingly recognized not just as passive energetic substrates but as regulatory signals. Cellular metabolites and reducing cofactors function as a dynamic "metabolic currency" that coordinates cell-autonomous adaptations with whole-organism physiology [6-8]. Despite these insights, the exact mechanistic channels through which localized alterations in nutrient partitioning actively dictate systemic endocrine signaling networks and organismal phenotypes remain poorly understood.

An important, yet underexplored, nexus linking metabolic remodeling to endocrine control is the availability of nicotinamide adenine dinucleotide phosphate (NADPH). This key reducing cofactor is universally required for both cellular redox homeostasis and the biosynthesis of lipophilic hormones, including steroids and juvenile hormones (JH) [9,10]. The rate-limiting terminal steps of these hormonal biosynthetic pathways frequently rely on cytochrome P450 monooxygenases, which exhibit an absolute dependence on a continuous supply of NADPH-derived reducing equivalents [11,12]. Classical endocrinology has mainly focused on the transcriptional regulation of these enzymes; however, whether

the upstream metabolic flux partitioning that feeds the intracellular NADPH pool can serve as **an important determinant of hormonal output** remains to be elucidated. One major metabolic engine generating cellular NADPH is the oxidative branch of the pentose phosphate pathway (oxPPP), a conserved pathway frequently upregulated during stress responses [13,14]. Because shunting glucose-derived carbon into the oxPPP diverts resources away from ATP-generating pathways, sustained oxPPP activation represents a fundamental bioenergetic trade-off. This metabolic reallocation may prioritize immediate endocrine and antioxidant defense adaptations at the expense of long-term energetic resilience and longevity [15,16].

The western honey bee, *Apis mellifera*, offers an exceptional and tractable non-mammalian social model to interrogate this behavior–metabolic–endocrine interface. In honey bee societies, individual workers exhibit profound behavioral plasticity, transitioning from in-hive nursing to out-hive foraging. This complex behavioral maturation is orchestrated by systemic titers of juvenile hormone (JH)—a lipid-soluble hormone synthesized via NADPH-dependent enzymes and terminal cytochrome P450-mediated reactions [17-19]. Importantly, exposure to diverse environmental challenges, including biotic factors like deformed wing virus (DWV) infection and abiotic stressors such as thermal fluctuations and agrochemicals [20,21], consistently triggers precocious foraging behaviors driven by elevated JH levels [22,23]. At the colony level, such premature behavioral transitions have the potential to disrupt social labor organization, illustrating how micro-level stress directly translates into macro-level social disruption[24,25]. This system therefore provides a unique opportunity to investigate how cell-intrinsic metabolic remodeling can be translated into endocrine regulation and socially relevant behavioral outcomes.

In this study, we demonstrate that carbon partitioning through the oxPPP acts as a **central metabolic-redox node** linking stress responses to systemic endocrine regulation and behavioral plasticity. Using ^{13}C stable isotope-tracing and flux-resolved metabolomics, we show that both pathogen-induced and environmental stresses prompt a major metabolic rewiring, redistributing glucose-derived carbon away from mitochondrial oxidation and shuffling it toward the high-turnover oxPPP. This sustained flux accumulation of oxPPP-derived NADPH directly fuels the cytochrome P450-dependent terminal epoxidation catalyzed by methyl farnesoate epoxidase (MFE), thereby accelerating JH biosynthesis. Furthermore, by implementing *in vivo* and *in vitro* functional perturbations with the oxPPP inhibitor DHEA (dehydroepiandrosterone), we successfully rescued the endocrine homeostasis and reversed the precocious behavioral timing, establishing a direct causal link between metabolic flux control and behavioral output. Together, our findings demonstrate that carbon partitioning through the oxPPP–NADPH axis constitutes an active regulatory mechanism rather than a passive consequence of stress adaptation. More broadly, these results establish a metabolic framework through which nutrient flux allocation can shape endocrine output and behavioral state.

Results

DWV infection induces metabolic and endocrine reprogramming

To determine how DWV infection reshapes host physiology, we characterized the temporal dynamics of metabolic and endocrine responses in honeybees. Longitudinal analysis revealed a pronounced disruption of glucose homeostasis within the central nervous system. Glucose levels in the heads of infected bees progressively declined from day 6 post-infection onward (Fig. 1A), indicating a reduction in glucose-derived carbon availability. Transcriptional profiling further supported this metabolic remodeling. At day 6 post-infection, DWV infection induced coordinated downregulation of genes involved in glycolysis, include Glyceraldehyde-3-phosphate dehydrogenase (*GAPDH*), Phosphoglycerate kinase (*PGK1*), Pyruvate kinase (*PK*) and the tricarboxylic acid (TCA) cycle include Isocitrate dehydrogenase (*ID*), Fumarate hydratase (*FH*), Succinate dehydrogenase (*SDH*), Succinate-CoA ligase (*SUCLA*), 2-oxoglutarate dehydrogenase (*Og*) (Fig. 1B, **Supplementary Table 1 and 2**), indicating reduced carbon flux through ATP-generating pathways. Consistent with this transcriptional reprogramming, ATP levels progressively declined from day 6 post-infection onward (Fig. 1C), suggesting the emergence of energetic stress within the brain. Together, these findings indicate that DWV infection suppresses central carbon metabolism and is associated with a substantial reduction in energy-generating capacity in the honeybee brain.

In parallel with these metabolic changes, DWV infection was accompanied by marked reorganization of endocrine signaling. At day 6 post-infection, genes involved in juvenile hormone (JH) biosynthesis include HMG-CoA synthase (*Hmgs*), HMG-CoA reductase (*Hmgr*), Isopentenyl pyrophosphate isomerase (*Ippi*), Farnesyl diphosphate (*Fpps*), Farnesal dehydrogenase (*FALD*), particularly the terminal enzyme methyl farnesoate epoxidase (*MFE*), were significantly upregulated in the head (Fig. 1D, Supplementary Table 3 and 4). In contrast, expression of the ecdysteroid-associated genes encoding cytochrome P450 enzymes—including 22-hydroxylase (*Disembodied/Dib/CYP302A1*), 2-hydroxylase (*Shadow/Sad/CYP315A1*), and 20-hydroxylase (*Shade/Shd/CYP314A1*)—was significantly reduced in the body (Fig. 1E, Supplementary Table 5 and 6). This reciprocal pattern of endocrine gene regulation suggests coordinated remodeling of JH- and ecdysteroid-associated signaling pathways during infection. Notably, increased *MFE* expression in the head coincided temporally with reduced *Shade/Shd/CYP314A1* expression in the body (Fig. 1F), revealing a pronounced divergence in endocrine regulation. Importantly, day 6 post-infection emerged as a critical physiological transition point at which the onset of energetic stress coincided with substantial endocrine remodeling. Subsequent mechanistic analyses therefore focused on this time point. Collectively, these results demonstrate that DWV infection induces coordinated metabolic and endocrine reprogramming, characterized by reduced carbon allocation toward ATP production and simultaneous activation of hormone biosynthetic pathways. These observations suggest that infection-driven changes in carbon partitioning may contribute to a premature shift toward a maturation-associated physiological state (Fig. 1G).

DWV infection reorganizes central carbon metabolism toward oxPPP activation

To define the metabolic pathways underlying the physiological transition identified above, we focused on day 6 post-infection. Longitudinal analyses revealed that day 6 represented a critical physiological nexus at which metabolic and endocrine disruptions coincided, characterized by the simultaneous emergence

of reduced glucose availability, decreased ATP levels, and the induction of JH-associated biosynthetic genes (Fig. 1). We therefore selected this time point for subsequent mechanistic analyses because it marked the transition from early infection to coordinated metabolic and endocrine remodeling. Consistent with the metabolic alterations observed in Fig. 1, glucose levels were significantly reduced in the heads of DWV-infected bees (Fig. 2A), accompanied by the coordinated downregulation of key genes involved in glycolysis and the tricarboxylic acid (TCA) cycle (Fig. 2B). These changes suggest reduced carbon flux through ATP-generating pathways in the central nervous system. Consistent with this interpretation, ATP levels were significantly reduced in DWV-infected heads (Fig. 2C, upper panel), accompanied by a modest increase in the ADP/ATP ratio (Fig. 2C, lower panel), indicating the emergence of energetic stress. To further evaluate mitochondrial oxidative metabolism, we quantified NADH, a key product of the TCA cycle and indicator of respiratory activity. NADH levels were significantly decreased in DWV-infected heads (Fig. 2D), supporting suppression of mitochondrial carbon oxidation and oxidative phosphorylation.

Pathway enrichment analysis further revealed significant enrichment of pentose phosphate pathway-associated processes and hormone signaling pathways, together with concurrent suppression of oxidative phosphorylation and TCA cycle pathways (Fig. 2E–G and Fig. S1B). **Given the limited biological replication of the RNA-seq dataset, transcriptomic observations were interpreted as pathway-level exploratory evidence and were independently validated by RT-qPCR, enzymatic activity measurements, stable isotope tracing, and pharmacological perturbation experiments.** These pathway-level changes suggest that glucose-derived carbon may be redirected away from mitochondrial ATP production toward alternative metabolic fates. To experimentally evaluate this possibility, we next examined the oxidative pentose phosphate pathway (oxPPP), the primary cellular source of NADPH. Although transcriptional induction of the rate-limiting oxPPP enzymes, glucose-6-phosphate dehydrogenase (*G6PD*) and 6-phosphogluconate dehydrogenase (*6PGD*), was statistically significant yet biologically modest (Fig. 2H), their corresponding enzymatic activities exhibited a far more pronounced increase in DWV-infected heads (Fig. 2I). This divergence indicates that while transcriptional regulation participates in the initial response, post-transcriptional or post-translational mechanisms heavily drive the robust functional activation of the oxPPP. Together, these findings demonstrate that DWV infection suppresses mitochondrial energy metabolism while actively accelerating oxPPP flux, consistent with a strategic redistribution of glucose-derived carbon away from ATP-generating pathways and toward alternative metabolic programs.

Isotopic tracing reveals increased carbon flux through the oxPPP

To determine whether the metabolic changes identified in Fig. 2 reflect altered carbon partitioning, we performed ^{13}C-glucose stable isotope tracing in honeybee heads (Fig. 3A). Labeling of glucose-6-phosphate (G6P) was comparable between control and DWV-infected bees (Fig. 3B), indicating unchanged glucose uptake and initial phosphorylation. In contrast, 6-phosphogluconate (6PG) exhibited markedly increased isotopic enrichment in DWV-infected bees (Fig. 3C and Supplementary Table 7), indicating enhanced channeling of glucose-derived carbon into the oxidative, NADPH-generating branch

of the PPP. Strikingly, propagation of increased flux through the oxPPP was non-uniform. Ribulose-5-phosphate (Ru5P) showed reduced steady-state abundance but increased isotopic enrichment (Fig. 3D), indicating rapid turnover. In contrast, ribose-5-phosphate (R5P) exhibited a significant and simultaneous increase in both abundance and isotopic enrichment (Fig. 3E). This divergence has important physiological implications. The reduced abundance but increased isotopic enrichment of Ru5P is consistent with increased flux through the oxPPP and enhanced NADPH production during infection. In contrast, the simultaneous increase in both abundance and isotopic enrichment of R5P suggests greater carbon entry into downstream pentose phosphate metabolism. This redistribution may increase the availability of ribose precursors for nucleotide biosynthesis, potentially supporting viral replication or host transcriptional remodeling.

The impact of DWV infection on energy-producing pathways was highly selective. Labeling of glyceraldehyde-3-phosphate (G3P) was reduced (Fig. 3G), whereas downstream glycolytic intermediates —including 3-phosphoglycerate (3PG)/2-phosphoglycerate (2PG), phosphoenolpyruvate (PEP), pyruvate, and lactate—showed comparable enrichment between groups (Fig. S2E–I), indicating preserved flux through lower glycolytic despite carbon diversion to the oxPPP. In contrast, a major bottleneck was observed at mitochondrial entry. Citrate/isocitrate and malate showed significantly reducing labeling (Fig. 3H–I), and additional TCA intermediates—including aconitate, α-ketoglutarate, succinate, and fumarate—also exhibited decreased isotopic enrichment (Fig. S2J–M). Time-resolved tracing further confirmed sustained suppression of mitochondrial carbon flux in infected bees.

Taken together, these flux-resolved analyses reveal that DWV infection actively redirects glucose-derived carbon toward a high-turnover oxPPP axis. This reprogramming establishes the oxPPP as a dominant carbon sink, prioritizing reductive and biosynthetic demands over ATP production, with the strongest attenuation of carbon flux occurring at the threshold of mitochondrial entry into oxidative metabolism.

PPP-mediated redox remodeling drives endocrine activation and behavioral maturation

Given that the oxPPP is the primary source of cellular reducing power, we examined whether the observed carbon flux reprogramming translates into systemic physiological effects. DWV infection significantly increased NADPH levels in the head at day 6 (Fig. 4A). Consistently, the $NADP^+$/NADPH ratio was significantly reduced (Fig. 4B), indicating a shift toward a more reduced intracellular redox state. Notably, total reactive oxygen species (ROS) levels were significantly reduced in a time- and dose-dependent manner (Fig. 4C). This counterintuitive result suggests that DWV-induced oxPPP activation increases NADPH availability beyond immediate antioxidant demand, potentially supporting downstream biosynthetic processes. We next examined whether this redox remodeling influences endocrine regulation. The terminal enzyme of juvenile hormone (JH) biosynthesis, methyl farnesoate epoxidase (MFE), was significantly upregulated at the transcriptional level in infected bees (Fig. 4D), accompanied by coordinated changes in upstream biosynthetic genes (Fig. S3A–E). Consistently, both HPLC and ELISA analyses showed a significant increase in systemic JH titers, particularly at day 6 post-infection

(Fig. 4E–F; Fig. S3G–H), indicating activation of the endocrine axis downstream of PPP-mediated redox remodeling.

Strikingly, this endocrine activation was accompanied by inverse regulation of key vitellogenesis-associated genes. Expression of three core vitellogenesis-related genes was significantly reduced in DWV-infected bees (Fig. S3F), highlighting a physiological trade-off between reproductive investment and JH-associated behavioral maturation. This reciprocal regulation is consistent with the well-established JH–vitellogenin regulatory network governing the transition from nursing to foraging in honeybees. To determine whether the terminal step of JH biosynthesis was altered following DWV infection, we performed an *in vitro* methyl farnesoate (MF)-to-JH conversion assay using crude head extracts. Head extracts prepared from control and DWV-infected bees at 6 days post-infection were incubated with methyl farnesoate under identical reaction conditions supplemented with exogenous NADPH. Under these conditions, extracts from DWV-infected bees produced significantly higher amounts of JH III than control extracts, indicating an enhanced capacity for the terminal conversion of methyl farnesoate to JH III (Fig. 4G). In contrast, both substrate-only blanks and heat-inactivated extract controls yielded negligible JH III production, confirming that product formation depended on enzymatically active components present in the head extracts.

At the organismal level, this oxPPP–redox–endocrine coupling was associated with accelerated behavioral maturation. Longitudinal tracking showed that DWV-infected bees initiated foraging significantly earlier than age-matched controls (Fig. 4H), indicating precocious behavioral transition. Collectively, these findings support a model in which DWV-induced oxPPP activation increases NADPH availability, facilitating the terminal step of JH biosynthesis and contributing to accelerated behavioral maturation in honeybees (Fig. 4I).

Functional perturbation and enzymatic validation establish PPP-derived NADPH as a causal regulator of juvenile hormone biosynthesis and behavioral maturation

To determine whether oxPPP activation causally drives DWV-induced physiological reprogramming, we performed targeted pathway perturbations. At the energetic level, ATP levels showed no significant differences among the four treatment groups [control, DWV, DHEA (dehydroepiandrosterone), and DWV+DHEA] at day 2. In contrast, group-specific differences emerged by day 6 (Fig. 5A), with DHEA treatment restoring ATP levels toward those of the control group. This metabolic recovery coincided with the rescue of endocrine and behavioral phenotypes, consistent with the restoration of central carbon metabolism following oxPPP inhibition. Stable ATP levels observed across all groups at day 2 further confirm that DHEA does not induce early global energy deficits or nonspecific toxicity.

Regarding oxPPP regulation, DWV infection increased both *G6PD* expression and its enzymatic activity, whereas DHEA, a competitive inhibitor of G6PD, effectively suppressed these responses (Fig. 5B and C), confirming successful modulation of PPP flux. Consistently, DWV-induced elevation of NADPH levels was markedly reduced by DHEA treatment (Fig. 5D), indicating targeted attenuation of oxPPP-derived reductive power. At the endocrine level, DWV infection significantly upregulated the expression of the

terminal JH biosynthetic enzyme MFE, an effect diminished upon oxPPP inhibition (Fig. 5E). Correspondingly, the DWV-induced increase in JH levels, measured independently by both HPLC and ELISA, was reversed by DHEA treatment (Fig. 5F and G), supporting a direct causal link between oxPPP activity and JH biosynthesis. At the behavioral level, DWV infection accelerated the transition to foraging, whereas DHEA treatment significantly delayed this shift (Fig. 5H, I), rescuing behavioral timing toward control levels. To determine whether increasing NADPH availability is sufficient to promote endocrine activation independently of viral infection, we supplemented uninfected bees with ribose and nicotinamide, which provide the carbon backbone and precursor required for NADPH generation. This intervention significantly elevated NADPH levels and increased systemic JH titers in the absence of infection (Fig. S4D–E), partially phenocopying the endocrine state observed in DWV-infected bees. Together with the inhibitory effects of DHEA and the NADPH-dependent stimulation of MFE activity observed in vitro, these findings support a functional role for NADPH availability in regulating JH biosynthesis in vivo and further implicate the oxPPP–NADPH axis as a key metabolic determinant of endocrine activation. To assess whether this response reflects a broader stress-responsive program, we examined additional environmental stressors. Both thermal stress and pesticide exposure (propargite) significantly increased G6PD activity (Fig. 5J) and NADPH levels (Fig. 5K), recapitulating the metabolic and redox phenotype observed during DWV infection. Altogether, these findings suggest that oxPPP activation and redox remodeling constitute a conserved core metabolic response to diverse stressors. Viral pathogens may exploit this generalized stress-responsive node to drive endocrine reprogramming and shift host behavior toward precocious foraging.

Discussion

Infection-associated metabolic reprogramming is widely recognized across host–pathogen systems, yet how these metabolic changes are translated into endocrine and behavioral outcomes remains poorly understood. Here, we identify a metabolic–endocrine axis linking pathogen-induced carbon reallocation to behavioral perturbation in honeybees. Specifically, DWV infection redirects glucose-derived carbon toward the oxPPP, increasing NADPH availability and supporting juvenile hormone biosynthesis, thereby promoting precocious behavioral maturation. JH is a well-established regulator of honeybee division of labor, and DWV infection has been associated with precocious foraging and altered worker behavior [17,18,26]. Previous studies have also shown that DWV infection disrupts brain energy metabolism, neurological function, and immune–metabolic balance in honeybees [27,28]. The honeybee–DWV host–pathogen system therefore provides a suitable platform for investigating how pathogen-induced metabolic remodeling is coupled to endocrine regulation and behavioral perturbation. Together, these findings establish the honeybee–DWV system as a tractable invertebrate model for investigating how stress-induced carbon partitioning regulates endocrine function and behavioral plasticity, with potential relevance to conserved NADPH-dependent endocrine systems.

A central feature of this metabolic reorganization was the redistribution of carbon flux toward the oxPPP. Reduced ATP and NADH levels (Fig. 2C–D), together with suppression of glycolytic and TCA cycle-

associated genes (Fig. 2B), indicate attenuation of oxidative metabolism in the honeybee head. Pathway enrichment analysis (Fig. 2E) and isotope tracing (Fig. 3C–E) further demonstrate preferential channeling of glucose-derived carbon into the oxPPP, accompanied by accelerated ribulose-5-phosphate turnover and accumulation of ribose-5-phosphate. These findings indicate that infection redirects carbon partitioning toward reductive and biosynthetic metabolism rather than ATP production, potentially supporting both host adaptation and viral replication.

Beyond its established antioxidant role [29], our results suggest that oxPPP-derived NADPH also contributes to endocrine regulation. Increased NADPH levels (Fig. 4A) and a reduced $NADP^+$/NADPH ratio (Fig. 4B) were accompanied by lower ROS levels (Fig. 4C), indicating that reducing equivalents accumulate beyond immediate antioxidant demand and become available for NADPH-dependent biosynthetic processes. Because the terminal step of juvenile hormone biosynthesis depends on an NADPH-dependent cytochrome P450 enzyme, increased NADPH availability may facilitate endocrine activation. Consistent with this model, DWV infection increased MFE expression and systemic JH titers (Fig. 4D–F), whereas pharmacological inhibition of the oxPPP suppressed both NADPH accumulation and JH production (Fig. 5D–G). Furthermore, NADPH enhanced methyl farnesoate-to-JH conversion in crude head extracts (Fig. 4G), supporting the conclusion that oxPPP-derived reducing power facilitates the terminal step of JH biosynthesis and links intracellular carbon partitioning with endocrine activation.

An important finding of this study is that transcriptional changes alone did not fully explain the observed metabolic and endocrine phenotypes. Although G6PD transcripts showed only modest induction (Fig. 2H), G6PD enzymatic activity increased substantially (Fig. 2I), indicating that oxPPP activation is likely regulated beyond the transcriptional level. Post-translational regulation of G6PD, including phosphorylation, has been reported in other systems [30] and may contribute to this discrepancy. Consistent with this possibility, DWV infection was accompanied by ATP depletion and increased AMPK phosphorylation (Fig. S5), suggesting that energetic stress may promote oxPPP activation through AMPK-associated metabolic regulation. However, the mechanistic relationship between AMPK signaling and G6PD activation remains to be determined[31]. A similar principle was observed for endocrine regulation. Although DWV infection increased MFE expression and systemic JH levels (Fig. 4D–F), transcriptional changes across the JH biosynthetic pathway were relatively modest and did not show a sustained temporal increase (Fig. S3A–E; Fig. 1D(b)). These observations, together with the effects of oxPPP inhibition and NADPH supplementation, suggest that infection-induced JH elevation depends not only on transcriptional regulation but also on metabolic cofactor availability and enzyme function. More broadly, these findings highlight the importance of integrating transcriptomics with metabolic flux analysis, enzymatic assays, and functional perturbation when investigating stress-induced metabolic reprogramming.

The present study identifies day 6 post-infection as a critical physiological transition point at which metabolic remodeling becomes coupled to endocrine activation. At this stage, DWV-infected bees initiated out-hive activity earlier than control bees (Fig. 4H), consistent with elevated JH levels (Fig. 4E–F) and an accelerated transition toward a maturation-associated physiological state. However, earlier

out-hive activity should not be interpreted as a direct equivalent of complete behavioral maturation. In natural colonies, age-related division of labor comprises multiple sequential tasks that were not individually quantified in this study, and behavioral progression is strongly influenced by colony demography and social interactions[32]. Therefore, the observed phenotype is more appropriately interpreted as an infection-associated acceleration of behavioral transition rather than a complete recapitulation of normal age-related maturation. Nevertheless, the convergence of metabolic remodeling, increased NADPH production, elevated JH biosynthesis, and earlier out-hive activity at day 6 supports the conclusion that this time point represents a mechanistically meaningful physiological transition linking metabolism, endocrine regulation, and behavior.

Overall, our findings identify carbon partitioning through the oxidative pentose phosphate pathway as a mechanistic link connecting pathogen-induced metabolic remodeling with endocrine regulation and behavioral plasticity in honey bees. Rather than representing a passive metabolic consequence of infection, oxPPP activation emerges as an active regulatory process that coordinates intracellular redox balance with hormone biosynthesis and organismal behavior. Although the ecological significance of this response remains context dependent, oxPPP activation may represent either a host adaptive strategy or a physiological state exploited by DWV to promote viral fitness through altered behavioral timing. Future studies examining viral transmission, colony-level performance, and host fitness will be important for distinguishing between these possibilities. More broadly, the honeybee–DWV system provides an experimentally tractable invertebrate model for understanding how stress-responsive carbon partitioning and NADPH-dependent metabolism regulate endocrine function and behavioral plasticity across animal systems.

Methods

Honeybee rearing and collection

Western honeybees (*Apis mellifera*) were obtained from a local apiary in Taoyuan, Taiwan, and maintained in the experimental garden of the Department of Entomology, National Taiwan University. Honey bees were reared according to previously described methods [33] with slight modifications. To obtain age-matched workers, comb frames containing capped brood were removed from the hive and incubated in darkness at 33°C until adult emergence. Newly emerged worker bees were collected daily as previously described [33]. Collected workers were transferred to BugDorm cages (30 × 30 × 30 cm; MegaView Science, Taiwan) and maintained in a temperature-controlled incubator at 33°C under dark conditions. Bees were provided with 0.7 M sucrose solution ad libitum, which was replaced daily.

Virus infection assay

Deformed wing virus (DWV)-containing extracts were prepared from *Varroa destructor* mite homogenates using a procedure modified from a previous study [34]. Briefly, 10 mites were homogenized in 100 µL of PBS and centrifuged at 12,000 × g for 10 min at 4 °C. The clarified supernatant was

collected and stored at –80 °C until use [35,36]. Viral concentrations, expressed as genome equivalents, were determined by quantitative PCR (qPCR) using a standard curve established in our previous study [27]. Only extracts with DWV copy numbers at least 1,000-fold higher than the target inoculation dose were selected and diluted for subsequent inoculation. Newly emerged worker bees were anesthetized on ice prior to injection. Each bee was injected with 1×10^4 viral copies of DWV into the thoracic hemocoel through the dorsal thorax using a microneedle injector to establish experimental infection. Control bees were injected with an equal volume of phosphate-buffered saline (PBS). After injection, bees were maintained in BugDorm cages (30 × 30 × 30 cm; MegaView Science, Taiwan) in a temperature-controlled incubator at 33°C and supplied with 0.7 M sucrose solution ad libitum. Bees were collected at 2 and 6 day-post-infection for subsequent analyses, including carbohydrate quantification, gene expression analysis, and biochemical assays.

RNA extraction, cDNA synthesis, and RT-qPCR analysis

Honeybee samples were collected for gene expression analysis and divided into control and DWV-infected groups. For tissue-specific analysis, heads and bodies were separated prior to RNA extraction. Total RNA was extracted from each sample using TRIzol reagent (Thermo Fisher Scientific, USA) according to the manufacturer's instructions. Briefly, tissues were homogenized in TRIzol reagent, followed by phase separation with chloroform (0.2 mL chloroform per 1 mL TRIzol). After incubation at room temperature for 5 min, samples were centrifuged at 12,000 ×g at 4°C for 15 min. The aqueous phase was transferred to a new tube and mixed with equal volume of isopropanol for RNA precipitation, followed by centrifugation at 12,000 ×g at 4°C for 10 min. RNA pellets were washed with 75% ethanol, centrifuged at 7,500 ×g at 4°C for 5 min, air-dried, and resuspended in DEPC-treated water. RNA concentration and purity were measured using a NanoDrop 2000 spectrophotometer (Thermo Scientific, USA), and RNA samples were stored at −80°C until use.

For cDNA synthesis, 500 ng of total RNA was reverse-transcribed using the SuperScript® III First-Strand Synthesis SuperMix (Thermo Fisher Scientific, USA) according to the manufacturer's protocol. Reverse transcription was performed using a thermal cycler (Biometra, Germany), and the synthesized cDNA was stored at −20°C for subsequent analysis. Quantitative real-time PCR (RT-qPCR) was performed using SYBR Green chemistry to determine relative gene expression levels. The 18S rRNA gene was used as the internal reference for normalization. Primers targeting genes involved in glycolysis, the tricarboxylic acid (TCA) cycle, the pentose phosphate pathway (PPP), and juvenile hormone biosynthesis were used for gene expression analysis. Primer sequences used in this study are listed in **Supplementary Table 8**. Relative gene expression levels were calculated using the $2^{-\Delta\Delta Ct}$ method [37].

Recording of behavioral transition of honeybees

Newly emerged honeybees were collected and artificially infected as previously described. After injection, bees were marked individually on the dorsal abdomen using acrylic paint and returned to their original hive maintained at the experimental apiary for behavioral observation under natural colony

conditions. The initiation of out-hive activity of marked bees was recorded daily during three times windows: 10:00–11:00, 13:00–14:00, and 15:00–16:00. The first day on which each marked bees were observed outside the hive was recorded, and the number of marked bees observed per day was also recoded.

Analysis of glucose and ATP content

Glucose content in honeybee head tissues and hemolymph was measured using a colorimetric glucose assay kit (Cell Biolabs, Inc., USA) according to the manufacturer's instructions. The reaction mixture consisted of 10 μL colorimetric probe, 2 μL horseradish peroxidase (HRP), 20 μL glucose oxidase, and 968 μL 1× assay buffer. For head tissue samples, tissues were homogenized and centrifuged at 10,000 ×g at 4°C for 10 min, and 10 μL of the supernatant was diluted with 1× assay buffer to a final volume of 50 μL. Hemolymph samples (10 μL per sample; pooled from three bees, n = 4) were prepared in the same manner. Standards and samples (50 μL each) were added to a 96-well plate, followed by 50 μL of reaction mixture, and incubated at 37°C for 30–45 min in the dark. Absorbance was measured at 540 nm using a microplate reader. ATP content in honeybee head tissues and hemolymph was measured using the ATP Determination Kit (Molecular Probes, USA) following the manufacturer's instructions. Samples were homogenized and centrifuged at 7,500 ×g at 4°C for 1 min, and 10 μL of the supernatant was transferred into a black 96-well microplate. The reaction mixture consisted of distilled water, 20× reaction buffer, 0.1 M DTT, 10 mM D-luciferin, and firefly luciferase. ATP standards were prepared in parallel using the same reaction mixture. The luminescence reaction was carried out at 28°C, and relative luminescence units (RLU) were measured using a microplate luminometer. ATP levels in the control group were set as 100% for normalization and comparison.

NADH, NADPH, and $NADP^+$ quantification

NADH, NADPH, and $NADP^+$ levels in honeybee head tissues were quantified using the NAD/NADH-Glo™ Assay and NADP/NADPH-Glo™ Assay (Promega, Madison, WI, USA) according to the manufacturer's instructions. Briefly, honeybee heads were collected at the indicated time points and immediately homogenized in the extraction buffer supplied with each assay. Homogenates were centrifuged at 12,000 × g for 10 min at 4°C, and the resulting supernatants were collected for analysis. For NADH quantification, samples were processed using the NAD/NADH-Glo™ Assay to selectively detect reduced NADH. For NADPH and $NADP^+$ quantification, parallel samples were analyzed using the NADP/NADPH-Glo™ Assay. To distinguish oxidized ($NADP^+$) and reduced (NADPH) forms, aliquots of each sample were subjected to differential decomposition according to the manufacturer's protocol. Total NADP ($NADP^+$ + NADPH) and NADPH were measured separately, and $NADP^+$ levels were calculated by subtracting NADPH from total NADP. Following the addition of the detection reagent, samples were incubated at room temperature for the recommended duration, and luminescence was measured using a microplate luminometer. Metabolite concentrations were calculated from standard curves generated using the corresponding standards supplied with each assay. The intracellular redox state was evaluated by calculating the $NADP^+$/NADPH ratio. All values were normalized to tissue weight and expressed relative

to the corresponding control group. Each biological replicate consisted of an individual honeybee head tissue homogenate, and four to five independent biological replicates were analyzed for each treatment group.

RNA sequencing and transcriptome analysis

For transcriptome profiling, total RNA from honeybee heads was extracted and quantified at 6 days post-infection as described above. Only high-quality RNA samples meeting strict purity thresholds (both A_{260}/A_{230} and A_{260}/A_{280} ratios >1.8) were selected for subsequent library preparation. Two independent biological replicates were included for each experimental group: day 0 control, day 6 control, and day 6 DWV. To construct the sequencing libraries, poly(A) mRNA was enriched using oligo(dT) beads and subsequently fragmented into short inserts. First-strand cDNA was synthesized utilizing random hexamer primers, followed by second-strand cDNA synthesis. After sequential end repair, A-tailing, adaptor ligation, and PCR amplification, the resulting cDNA libraries were purified and rigorously quantified. Sequencing was performed on an Illumina NovaSeq 6000 platform (Illumina, San Diego, CA, USA) to generate 150 bp paired-end reads. Raw sequencing reads were subjected to stringent quality control filtering to remove adaptor sequences, ambiguous bases (N), and low-quality reads, thereby yielding clean reads. These clean reads were mapped to the *Apis mellifera* reference genome using STAR (v2.7.9a)[38]. Gene-level raw read counts were enumerated simultaneously during alignment and subsequently input into the DESeq2 package for differential expression analysis[39]. Genes with low read counts (e.g., FPKM < 1 in all replicates) were filtered out prior to downstream analysis. Differentially expressed genes (DEGs) between the control and DWV-infected groups were identified based on the thresholds of an adjusted *P* value<0.05 and a $\log_2$ fold change>1. For downstream transcript abundance quantification and visualization, read counts were normalized as fragments per kilobase of transcript per million mapped reads (FPKM). Functional annotation and pathway dynamics were evaluated via Gene Set Enrichment Analysis (GSEA) and Kyoto Encyclopedia of Genes and Genomes (KEGG) pathway enrichment analyses to identify significantly altered metabolic and signaling networks. Representative heatmaps illustrating the transcriptional profiles of genes associated with glycolysis, the tricarboxylic acid (TCA) cycle, and the pentose phosphate pathway (PPP) were constructed using $\log_2$-transformed FPKM values.

Measurement of G6PD and 6PGD enzymatic activities

The enzymatic activities of glucose-6-phosphate dehydrogenase (G6PD) and 6-phosphogluconate dehydrogenase (6PGD) in honeybee head tissues were measured using the Glucose-6-Phosphate Dehydrogenase Activity Assay Kit and the 6-Phosphogluconate Dehydrogenase Activity Assay Kit (Abcam, Cambridge, UK) according to the manufacturer's instructions. Briefly, honeybee heads were collected at the indicated time points and homogenized in ice-cold assay buffer supplied with each kit. Homogenates were centrifuged at 12,000 × g for 10 min at 4°C, and the resulting supernatants were collected for enzyme activity analysis. Reaction mixtures containing the appropriate assay reagents and tissue extracts were prepared according to the manufacturer's protocol and incubated at 37°C for the

recommended duration. Enzymatic activities were determined by measuring NADPH generation using a colorimetric assay at 450 nm with a microplate reader. Enzyme activities were calculated according to the manufacturer's instructions and normalized to total protein concentration. Relative enzymatic activities were expressed as fold changes relative to the corresponding control group. Each biological replicate consisted of a single honeybee head extract, and four to five independent biological replicates were analyzed for each treatment group.

Stable isotope tracing by oral feeding of ^{13}C-glucose

To investigate the redistribution of glucose-derived carbon flux during DWV infection, stable isotope tracing was performed by incubating the tissues with uniformly labeled ^{13}C-glucose. Control and DWV-infected bee brains at 6 days post-infection were dissected and incubated in external solution (140 mM NaCl, 50 mM KCl, 1 mM MgCl2, 2.5 mM CaCl2, 4 mM NaHCO3, 1.2 mM NaH2PO4, 6 mM HEPES, 5 mM U-$^{13}C_6$-labeled glucose, pH adjusted to 7.4 using NaOH) [40] and uniformly labeled for 1 h as the metabolic labeling period. After labeling, the brains were immediately collected, flash-frozen in liquid nitrogen, and stored at −80°C until metabolite extraction. For metabolite extraction, head tissues were homogenized in pre-chilled extraction solvent (methanol:acetonitrile:water, 2:2:1, v/v/v) and centrifuged at 15,000 ×g for 15 min at 4°C. The supernatants were collected and dried under vacuum, and the dried extracts were reconstituted in appropriate solvent for metabolite analysis. Metabolite profiling and isotopologue analysis were performed using liquid chromatography–mass spectrometry (LC–MS) on a quadrupole time-of-flight (QTOF) mass spectrometer (Agilent Technologies, USA). Metabolites involved in glycolysis, the pentose phosphate pathway (PPP), and the tricarboxylic acid (TCA) cycle were analyzed, including glucose-6-phosphate (G6P), 6-phosphogluconate (6PG), ribulose-5-phosphate (Ru5P), ribose-5-phosphate (R5P), glyceraldehyde-3-phosphate (G3P), citrate/isocitrate, and malate. The isotopologue distributions (m+0 to m+n) were determined based on mass shifts corresponding to ^{13}C incorporation. Fractional enrichment of each isotopologue was calculated as the proportion of labeled metabolites relative to total metabolite abundance to evaluate glucose-derived carbon redistribution under DWV infection conditions.

DHEA treatment and pharmacological inhibition of the pentose phosphate pathway

To investigate the functional role of pentose phosphate pathway (PPP) activity in DWV-induced metabolic and endocrine reprogramming, honeybees were treated with dehydroepiandrosterone (DHEA), a competitive inhibitor of glucose-6-phosphate dehydrogenase (G6PD). Newly emerged worker bees were randomly assigned to four treatment groups: control, DWV infection, DHEA treatment alone, and DWV + DHEA co-treatment. For DHEA administration, DHEA (Sigma-Aldrich, USA) was dissolved in dimethyl sulfoxide (DMSO) as a stock solution, prior to the main experiments, 2.5, 5, and 10 μM DHEA were evaluated, and 2.5 μM was selected based on its ability to significantly increase head ATP levels on day 6 (Supplementary Figure 4). DHEA was diluted in 0.7 M sucrose solution to a final concentration of 2.5 μM and fed to honeybees *ad libitum* daily throughout the experimental period. Control groups were the bees fed with equivalent sucrose only. For the combined treatment group, bees were first injected

with DWV (1×10^4 viral copies per bee) as described above and subsequently fed the DHEA-containing sucrose solution. Honeybee head tissues were collected at 2 and 6 days post-treatment for analysis of ATP levels, G6PD expression and enzymatic activity, NADPH levels, and juvenile hormone biosynthesis-related gene expression. Behavioral transition to out-hive activity was monitored under colony conditions as described in the field release assay.

ROS quantification

Total reactive oxygen species (ROS) levels in honey bee hemolymph were quantified using a DCFDA-based fluorometric assay [41]. Tris buffer (10 mM, pH 7.2 adjusted with HCl) was used as the assay buffer. Hemolymph was collected from two anesthetized bees, and 5 µL was pooled and diluted with 85 µL of assay buffer. Hydrogen peroxide (H_2O_2) standards (0–7 mM) were prepared in assay buffer, and 5 µL of each standard was used to generate a standard curve. For ROS detection, 10 µL of DCFDA solution (1 mM) was added to each sample, followed by incubation at 26 °C for 10 min. Fluorescence intensity was measured at excitation/emission wavelengths of 485/535 nm using an Infinite F Nano+ microplate reader (Tecan Life Science, Männedorf, Switzerland).

***In vitro* MFE activity assay**

To determine whether NADPH availability supports the terminal epoxidation step of juvenile hormone biosynthesis, an *in vitro* enzyme activity assay was performed using crude head extracts prepared from individual honeybees. Head tissues from the control and DWV-infected groups at day 6 post-infection were collected and homogenized individually in ice-cold phosphate-buffered saline (0.1 M, pH 7.4). Homogenates were centrifuged at 12,000 × *g* for 10 min at 4°C, and the resulting supernatants were collected as crude enzyme extracts. The standard 200 µL reaction mixture contained crude extract prepared from a single honeybee head, 20 µM methyl farnesoate, and 1 mM NADPH added immediately before incubation. Negative control reactions included a substrate-only blank and heat-inactivated crude extracts (95°C for 5 min) to confirm that JH III formation was strictly dependent on active enzymatic machinery. Reactions were incubated at 30°C for 30 min and terminated by adding an equal volume of ice-cold ethyl acetate. Synthesized juvenile hormone III was extracted into the organic phase, clarified by centrifugation, dried under nitrogen gas, and re-dissolved in the assay buffer provided with the ELISA kit. The amount of newly synthesized JH III was quantified using a commercial juvenile hormone ELISA kit according to the manufacturer's instructions. At least five individual honeybees were analyzed as independent biological replicates for each experimental condition, and relative methyl farnesoate epoxidation activity was normalized to the control group.

Quantification of juvenile hormone by HPLC and ELISA

Juvenile hormone (JH) levels in honeybee hemolymph were quantified using both high-performance liquid chromatography (HPLC) and enzyme-linked immunosorbent assay (ELISA) (Lifeasible, Shirley, NY, USA). For HPLC analysis, JH quantification was performed using a Hitachi D-2000 Elite HPLC system (Hitachi, Japan) equipped with a CAPCELL PAK UG120 CN column (Osaka Soda, Japan). Detection was

carried out at 217 nm using UV absorbance at a flow rate of 0.2 mL/min. Juvenile hormone III (JH III; Sigma-Aldrich, USA) was used as the standard for quantification. A stock solution of JH III was prepared in dimethylformamide (DMF), followed by serial dilution to generate a standard curve. For sample preparation, 20 μL of honeybee hemolymph was mixed with 80 μL of DMF and vortexed thoroughly. An aliquot of 10 μL of each sample was injected into the HPLC system. JH concentrations were determined by comparing peak areas with the JH III standard curve. For ELISA analysis, JH levels were additionally quantified using a commercial juvenile hormone ELISA kit according to the manufacturer's instructions. Briefly, hemolymph samples were collected and diluted in the assay buffer provided by the kit. Standards and samples were added to ELISA plates pre-coated with JH-specific antibodies and incubated under the recommended conditions. After washing, enzyme-conjugated secondary antibodies and substrate solution were added for color development. The reaction was terminated using stop solution, and absorbance was measured at 450 nm using a microplate reader. JH concentrations were calculated based on the standard curve generated with known JH standards. Both methods were used independently to validate JH quantification, and the resulting values were used for comparative analyses among experimental groups.

Thermal and pesticide stress treatments

To determine whether pentose phosphate pathway (PPP) activation represents a general stress-responsive metabolic program, honeybees were subjected to thermal stress or pesticide treatment. Newly emerged worker bees were randomly assigned to control, thermal stress, and pesticide treatment groups. For thermal stress treatment, honey bees were transferred to an incubator maintained at 40°C for 2 h to induce acute heat stress. After treatment, bees were returned to standard rearing conditions (33°C) for recovery. Head tissues were collected at the indicated time points for subsequent measurement of G6PD enzymatic activity and NADPH levels. For pesticide treatment, propargite (Sigma-Aldrich, USA) was diluted 1:9000 in 0.7 M sucrose solution and administered orally to honey bees by feeding [42]. Control bees were fed sucrose solution without pesticide. After exposure, honeybee heads were collected at the indicated time points for biochemical analyses, including G6PD activity and NADPH quantification. These treatments were used to evaluate whether environmental stressors other than viral infection could induce metabolic reprogramming through PPP activation.

Statistical analysis

All statistical analyses were performed using GraphPad Prism 9.0 (GraphPad Software, USA). Differences between two groups were analyzed using unpaired Student's t-test, while comparisons among multiple groups were performed using one-way ANOVA. For behavioral survival analyses, cumulative out-hive activity was analyzed using the log-rank (Mantel–Cox) test. Post hoc multiple comparisons were performed when applicable. Data are presented as mean ± SD. Statistical significance was defined as $p < 0.05$. Different letters in the figures indicate statistically significant differences among treatment groups based on Tukey *post hoc* multiple comparison tests. Sample sizes for each experiment are provided in the corresponding figure legends.

Declarations

Data availability

The data supporting the findings of this study are available within the article and its Supplementary Information files. Additional datasets generated and analyzed during the current study are available from the corresponding author upon reasonable request.

Acknowledgements

We thank the RNAi Core Facility, Institute of Molecular Biology, Academia Sinica, Taiwan, for technical support.

Contributions

Y.-H.L., Y.-K.T., and Y.-L.W. conceived and designed the study. Y.-H.L., Y.-K.T., and W.-C.C. performed the experiments. Y.-H.L., Y.-K.T., and Y.-L.W. developed the methodology and analyzed the data. Y.-H.L. and Y.-K.T. prepared the figures and drafted the manuscript. Y.-L.W. supervised the study, secured funding, and provided resources. All authors contributed to data interpretation, reviewed the manuscript, and approved the final version.

References

1. Darweesh M, Mohammadi S, Rahmati M, Al-Hamadani M, Al-Harrasi A (2025) Metabolic reprogramming in viral infections: the interplay of glucose metabolism and immune responses. Front Immunol 16:1578202
2. Pérez SE, Gooz M, Maldonado EN (2024) Mitochondrial dysfunction and metabolic disturbances induced by viral infections. Cells 13:1789
3. Galenza A, Foley E (2019) Immunometabolism: insights from the Drosophila model. Dev Comp Immunol 94:22–34
4. Girdhar K et al (2021) Viruses and metabolism: the effects of viral infections and viral insulins on host metabolism. Annual Rev Virol 8:373–391
5. Thaker SK et al (2019) Differential metabolic reprogramming by Zika virus promotes cell death in human versus mosquito cells. *Cell metabolism* 29, 1206–1216. e1204
6. Koyama T, Saeed U, Rewitz K, Halberg K (2025) V. The integrative physiology of hormone signaling: Insights from insect models. Physiology 40:343–362
7. Erion R, Sehgal A (2013) Regulation of insect behavior via the insulin-signaling pathway. Front Physiol 4:353
8. Morton G, Cummings D, Baskin D, Barsh G, Schwartz M (2006) Central nervous system control of food intake and body weight. Nature 443:289–295

9. Chen L, Xing X, Zhang P, Chen L, Pei H (2024) Homeostatic regulation of NAD (H) and NADP (H) in cells. Genes Dis 11:101146
10. Riddick DS et al (2013) NADPH–cytochrome P450 oxidoreductase: roles in physiology, pharmacology, and toxicology. Drug Metab Dispos 41:12–23
11. Hamdane D, Zhang H, Hollenberg P (2008) Oxygen activation by cytochrome P450 monooxygenase. Photosynth Res 98:657–666
12. Helvig C, Koener J, Unnithan G, Feyereisen R (2004) CYP15A1, the cytochrome P450 that catalyzes epoxidation of methyl farnesoate to juvenile hormone III in cockroach corpora allata. *Proceedings of the National Academy of Sciences* 101, 4024–4029
13. Kazek M et al (2024) Glucose and trehalose metabolism through the cyclic pentose phosphate pathway shapes pathogen resistance and host protection in Drosophila. PLoS Biol 22:e3002299
14. Kazek M et al (2023) Metabolism of glucose and trehalose by cyclic pentose phosphate pathway is essential for effective immune response in Drosophila. *bioRxiv*, 2008. 2017.553657 (2023)
15. Moret Y, Schmid-Hempel P (2000) Survival for immunity: the price of immune system activation for bumblebee workers. Science 290:1166–1168
16. Libert S, Chao Y, Chu X, Pletcher SD (2006) Trade-offs between longevity and pathogen resistance in Drosophila melanogaster are mediated by NFκB signaling. Aging Cell 5:533–543
17. Sullivan JP, Jassim O, Fahrbach SE, Robinson GE (2000) Juvenile Hormone Paces Behavioral Development in the Adult Worker Honey Bee. Horm Behav 37:1–14. https://doi.org/10.1006/hbeh.1999.1552
18. Robinson GE (1987) Regulation of honey bee age polyethism by juvenile hormone. Behav Ecol Sociobiol 20:329–338
19. Robinson GE (2009) In: Vincent H, Resh, Ring T, Cardé (eds) Encyclopedia of Insects (Second Edition). Academic, pp 297–299
20. Benaets K et al (2017) Covert deformed wing virus infections have long-term deleterious effects on honeybee foraging and survival. *Proceedings of the Royal Society B: Biological Sciences* 284
21. Coulon M et al (2020) Interactions between thiamethoxam and deformed wing virus can drastically impair flight behavior of honey bees. Front Microbiol 11:766
22. Schulz DJ, Huang Z-Y, Robinson GE (1998) Effects of colony food shortage on behavioral development in honey bees. Behav Ecol Sociobiol 42:295–303. 10.1007/s002650050442
23. Corona M et al (2007) Vitellogenin, juvenile hormone, insulin signaling, and queen honey bee longevity. *Proceedings of the National Academy of Sciences* 104, 7128–7133
24. Perry CJ, Sovik E, Myerscough MR, Barron AB (2015) Rapid behavioral maturation accelerates failure of stressed honey bee colonies. Proc Natl Acad Sci U S A 112:3427–3432. 10.1073/pnas.1422089112
25. Khoury DS, Myerscough MR, Barron AB (2011) A quantitative model of honey bee colony population dynamics. PLoS ONE 6:e18491. 10.1371/journal.pone.0018491

26. Benaets K et al (2017) Covert deformed wing virus infections have long-term deleterious effects on honeybee foraging and survival. *Proceedings of the Royal Society B: Biological Sciences* 284. 10.1098/rspb.2016.2149
27. Chen P et al (2021) Deformed wing virus infection affects the neurological function of Apis mellifera by altering extracellular adenosine signaling. Insect Biochem Mol Biol 139:103674. https://doi.org/10.1016/j.ibmb.2021.103674
28. Becchimanzi A et al (2025) Deformed wing virus coopts the host arginine kinase to enhance its fitness in honey bees (Apis mellifera). BMC Biol 23. 10.1186/s12915-025-02117-x
29. Stanton RC (2012) Glucose-6-phosphate dehydrogenase, NADPH, and cell survival. IUBMB Life 64:362–369. https://doi.org/10.1002/iub.1017
30. Ma H et al (2021) c-Src facilitates tumorigenesis by phosphorylating and activating G6PD. Oncogene 40:2567–2580. 10.1038/s41388-021-01673-0
31. Jeon SM, Chandel NS, Hay N (2012) AMPK regulates NADPH homeostasis to promote tumour cell survival during energy stress. Nature 485:661–665. 10.1038/nature11066
32. Huang ZY, Robinson GE (1992) Honeybee colony integration: worker-worker interactions mediate hormonally regulated plasticity in division of labor. Proc Natl Acad Sci U S A 89:11726–11729. 10.1073/pnas.89.24.11726
33. Lu Y-H et al (2020) Identification of immune regulatory genes in Apis mellifera through caffeine treatment. Insects 11:516
34. Koleoglu G, Goodwin PH, Reyes-Quintana M, Hamiduzzaman MM, Guzman-Novoa E (2017) Effect of Varroa destructor, wounding and Varroa homogenate on gene expression in brood and adult honey bees. PLoS ONE 12:e0169669
35. Prayugo V, Payne AN, Bonning BC, Dolezal AG (2026) Infection timelines and co-infection effects of Israeli acute paralysis virus and deformed wing virus in the honey bee (Apis mellifera). J Invertebr Pathol 214:108484. https://doi.org/10.1016/j.jip.2025.108484
36. Cook SC et al (2023) Deformed wing virus of honey bees is inactivated by cold plasma ionized hydrogen peroxide. Front Insect Sci 3–2023. 10.3389/finsc.2023.1216291
37. Livak KJ, Schmittgen TD (2001) Analysis of relative gene expression data using real-time quantitative PCR and the 2 – ΔΔCT method. *methods* 25, 402–408
38. Dobin A et al (2013) STAR: ultrafast universal RNA-seq aligner. Bioinformatics 29:15–21. 10.1093/bioinformatics/bts635
39. Love MI, Huber W, Anders S (2014) Moderated estimation of fold change and dispersion for RNA-seq data with DESeq2. Genome Biol 15:550. 10.1186/s13059-014-0550-8
40. Palmer MJ et al (2013) Cholinergic pesticides cause mushroom body neuronal inactivation in honeybees. Nat Commun 4:1634. 10.1038/ncomms2648
41. Jambunathan N (2010) in *Plant Stress Tolerance: Methods and Protocols* (ed Ramanjulu Sunkar) 291–297Humana Press

42. Lin C-Y et al (2025) Synergistic impacts of propargite exposure and deformed wing virus infection on the health of western honey bees. Ecotoxicol Environ Saf 289:117430

Figures

Fig. 1

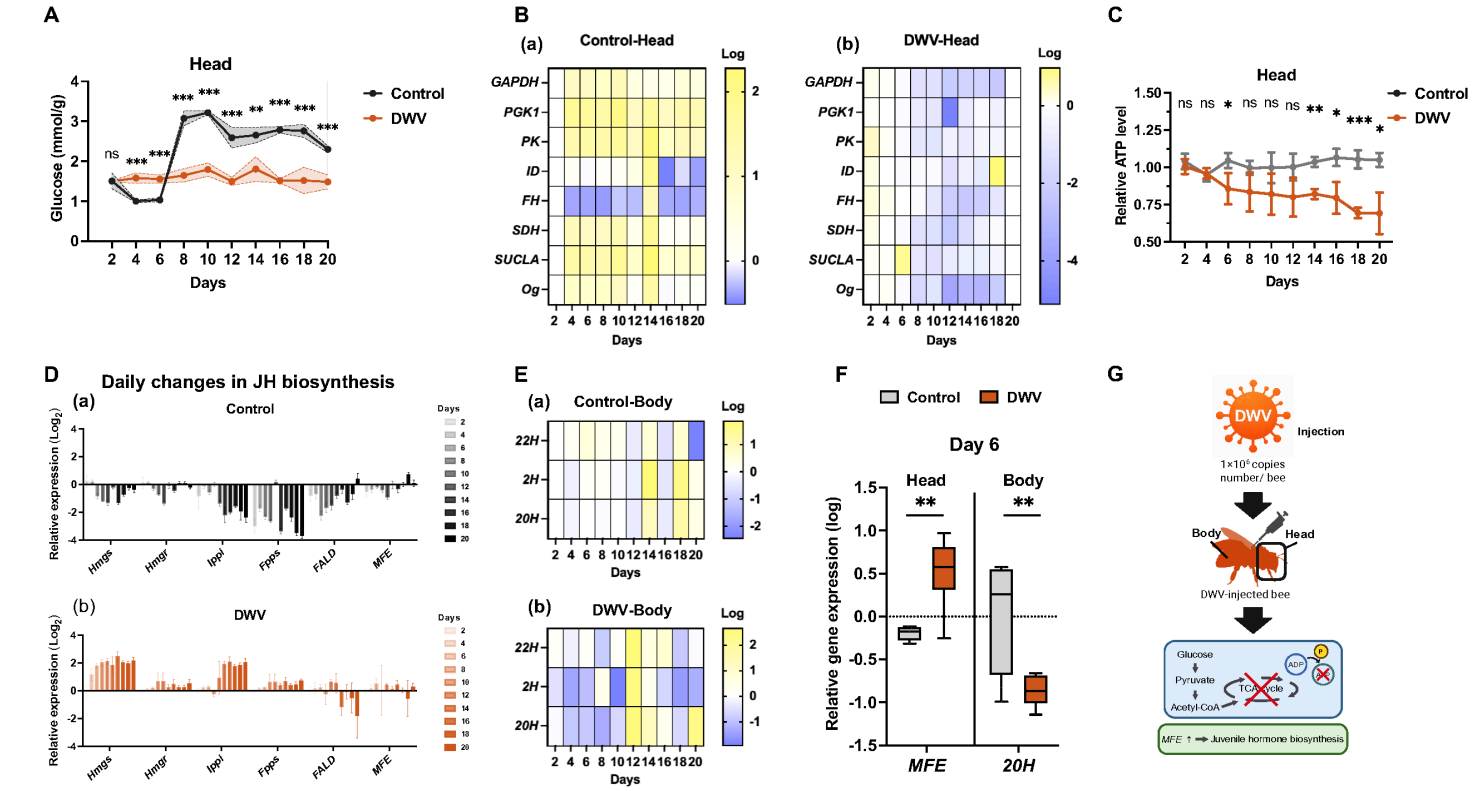


Figure 1

Temporal changes in glucose metabolism and hormone biosynthesis-related pathways in DWV-infected honeybees. (A) Daily changes in glucose levels in honeybee heads from day 2 to day 20 after DWV infection (n ≥ 4). (B) Heatmap showing relative gene expression levels of metabolic enzymes involved in glycolysis (*GAPDH*, *PGK1*, and *PK*) and the tricarboxylic acid (TCA) cycle (*ID*, *FH*, *SDH*, *SUCLA*, and *Og*) in honeybee heads from day 2 to day 20 in control (a) and DWV-infected (b) bees (n ≥ 3). (C) Daily changes in ATP levels in honeybee heads from day 2 to day 20 after DWV infection (n = 3). (D) Relative gene expression levels of enzymes involved in the juvenile hormone (JH) biosynthesis pathway (*Hmgs*, *Hmgr*, *Ippi*, *Fpps*, *FALD*, and *MFE*) from day 2 to day 20 in control and DWV-infected bees (n ≥ 6). (E)

Relative gene expression levels of ecdysteroid biosynthesis-related enzymes (i.e., *Dib/CYP302A1*, *Sad/CYP315A1*, and *Shd/CYP314A1*) in honeybee bodies from day 2 to day 20 in control (a) and DWV-infected (b) bees (n ≥ 5). (F) Comparison of *MFE* expression in heads and *Shd/CYP314A1* expression in bodies at day 6 in control and DWV-infected bees. (G) Schematic illustration of the experimental design. Honey bee heads (brain) and body tissues (thorax–abdomen)

were analyzed separately. Control bees were injected with PBS, and DWV-treated bees were injected with 1×10^4 viral copies per bee. All relative data are presented as fold changes normalized to day 2 within the same treatment group. Heatmaps and panel (F) show $\log_2$-transformed gene expression levels. Color intensity represents the magnitude of expression changes, with yellow indicating upregulation and blue indicating downregulation. Data are presented as mean ± SD. Statistical analyses were performed using Student's t-test or two-way ANOVA, as appropriate. Asterisks indicate statistical significance (*P < 0.05, **P < 0.01, ***P < 0.001, ****P < 0.0001).

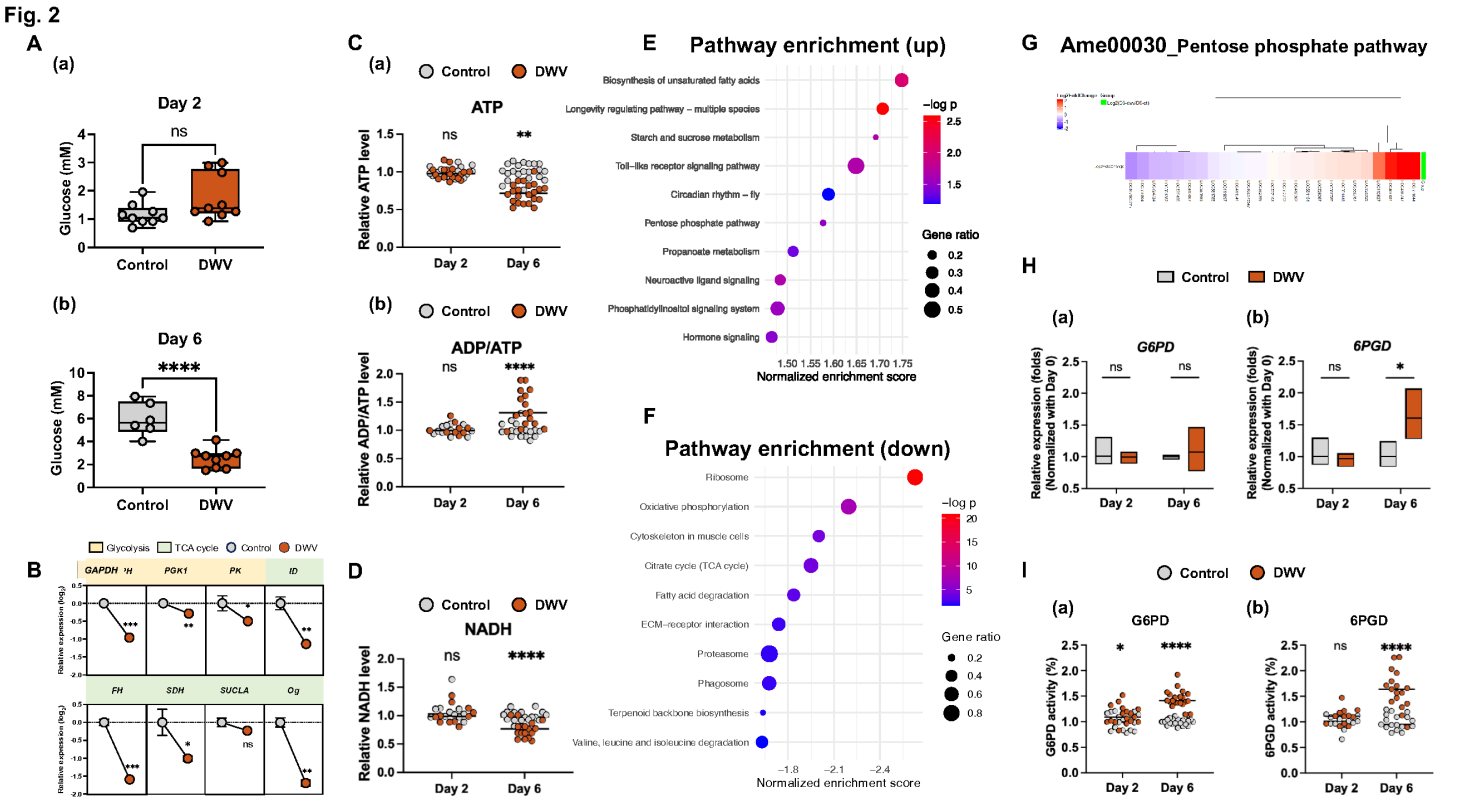


Figure 2

DWV infection alters energy metabolism and oxidative pentose phosphate pathway-related responses in honeybee heads. (A) Glucose levels in honeybee heads on day 2 (a) and day 6 (b) after DWV infection (n ≥ 6). (B) Relative gene expression levels of metabolic enzymes involved in glycolysis (*GAPDH*, *PGK1*, and *PK*) and the tricarboxylic acid (TCA) cycle (*ID*, *FH*, *SDH*, *SUCLA*, and *Og*) in honeybee heads on day 6 (n = 3). (C) Relative ATP levels (a) and ADP/ATP ratios (b) in honeybee heads on day 2 and day 6 after DWV infection (n ≥ 16, n ≥ 12). (D) Relative NADH levels in honeybee heads on day 2 and day 6 after DWV infection (n ≥ 11). (E, F) GSEA-based KEGG pathway enrichment analysis showing significantly upregulated (E) and downregulated (F) pathways in DWV-infected honeybee heads. The x-axis indicates the normalized enrichment score (NES). Dot size represents the gene ratio, and color indicates $-\log_{10}$ (p value). (G) Heatmap of differentially expressed genes associated with the pentose phosphate pathway (KEGG: Ame00030), showing $\log_2$-transformed fold changes relative to controls. (H) Relative gene expression levels of *glucose-6-phosphate dehydrogenase* (*G6PD*) (a) and *6-phosphogluconate*

dehydrogenase (*6PGD*) (b) in honeybee heads on day 2 and day 6 after DWV infection (n ≥ 4). (I) Enzymatic activity of G6PD (a) and 6PGD (b) in honeybee heads on day 2 and day 6 after DWV infection (n ≥ 10, n ≥ 11). Control bees were injected with PBS, and DWV-treated bees were injected with 1×10^4 viral copies per bee. Data in panel (H) were normalized to day 0, whereas all other relative data were normalized to the control group at the corresponding time point. Data are presented as mean ± SD. Statistical analyses were performed using Student's t-test or two-way ANOVA, as appropriate. Asterisks indicate significant differences (*P < 0.05, **P < 0.01, ***P < 0.001, ****P < 0.0001).

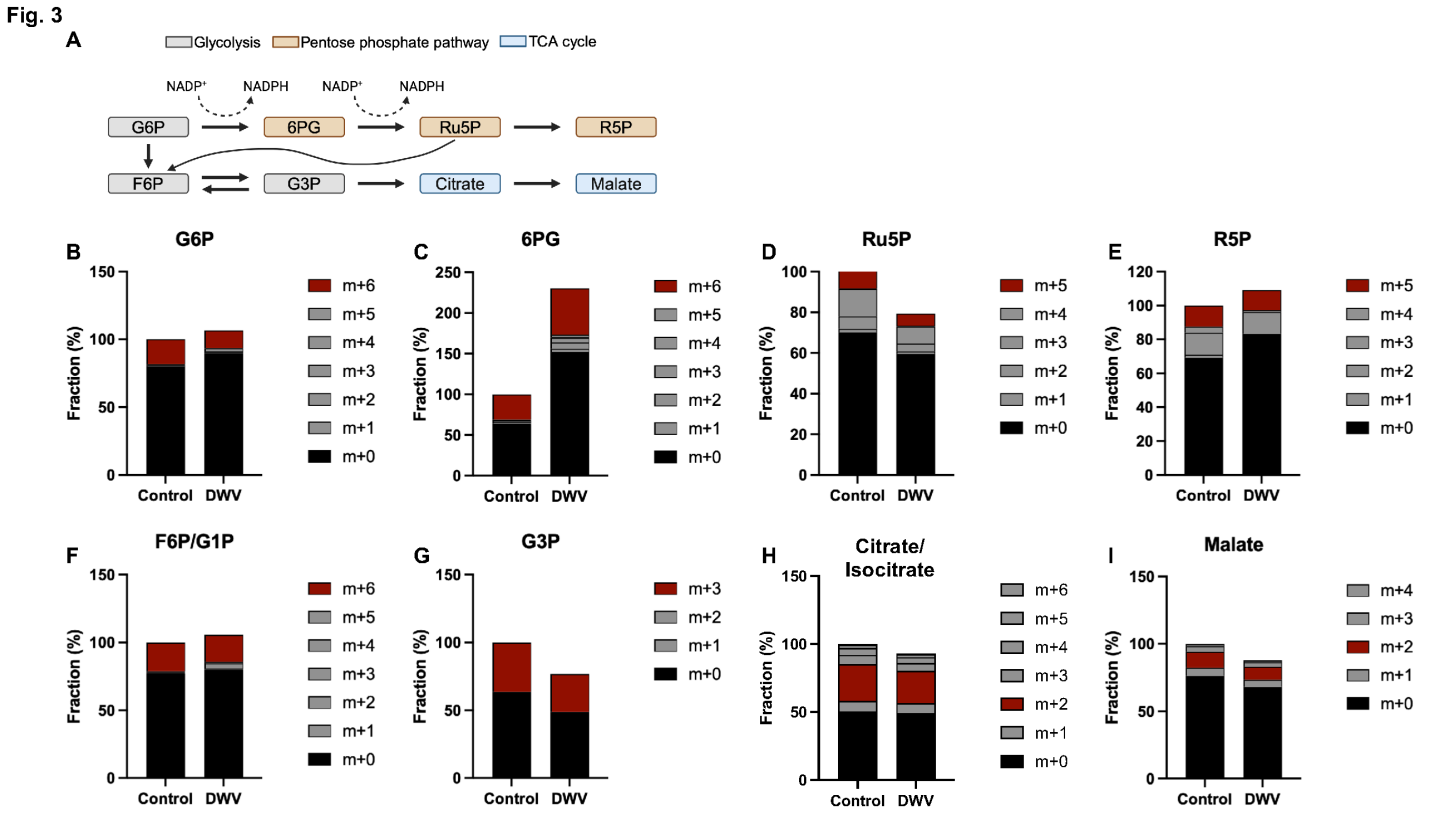


Figure 3

Stable ^{13}C-glucose tracing analysis of glucose-derived metabolic intermediates in DWV-infected honeybees. (A) Schematic illustration of metabolites in glucose metabolic pathways, including glycolysis (gray), the pentose phosphate pathway (PPP, brown), and the tricarboxylic acid (TCA) cycle (blue). (B–I) Isotopologue distributions of glucose-derived metabolites were analyzed by stable ^{13}C-glucose tracing in honeybees with or without DWV infection (n = 3). Fractional enrichment of labeled isotopologues (m+0 to m+6) is shown for intermediates in glycolysis and the pentose phosphate pathway (PPP), including glucose-6-phosphate (G6P), 6-phosphogluconate (6PG), ribulose-5-phosphate (Ru5P), ribose-5-phosphate (R5P), fructose-6-phosphate/glucose-1-phosphate (F6P/G1P), and glyceraldehyde-3-phosphate (G3P), as well as tricarboxylic acid (TCA) cycle metabolites, including citrate/isocitrate and malate. The m+0 fraction (black) represents unlabeled endogenous carbon, whereas the colored fractions indicate incorporation of ^{13}C-derived carbon from glucose into each metabolite. The red segment represents the highest labeled isotopologue detected for each metabolite.

Fig. 4

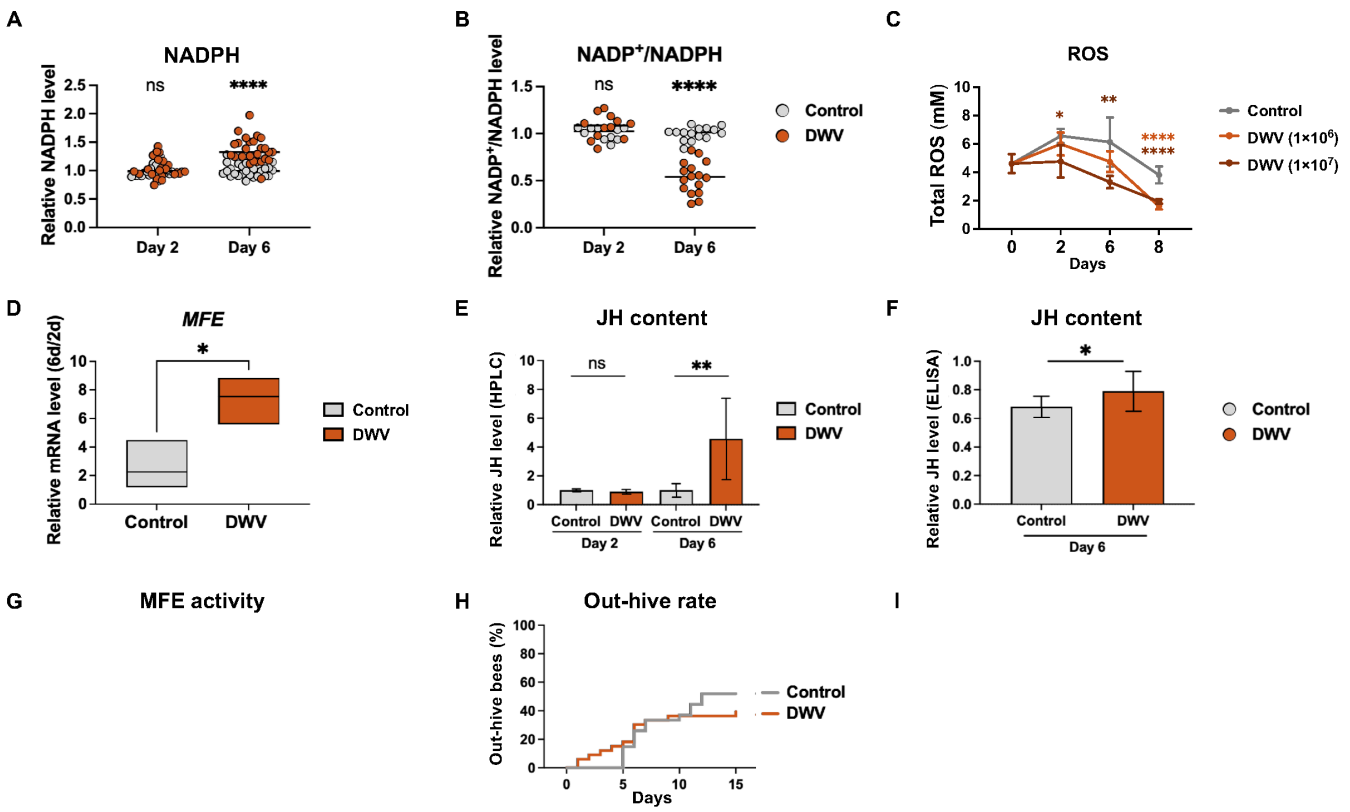


Figure 4

DWV infection alters redox metabolism, juvenile hormone biosynthesis, and foraging behavior in honeybees. (A) Relative NADPH levels in honeybee heads on day 2 and day 6 after DWV infection (n ≥ 21). (B) Relative $NADP^+$/NADPH ratios in honeybee heads on day 2 and day 6 after DWV infection (n ≥ 10). (C) Total reactive oxygen species (ROS) levels in honeybee heads from day 2 to day 8 after DWV infection (n ≥ 5). (D) Relative gene expression levels of *methyl farnesoate epoxidase* (*MFE*) in honeybee heads on day 6 (n ≥ 4). (E, F) Juvenile hormone (JH) levels in honeybees measured by HPLC on day 2 and day 6 (n ≥ 3) and by ELISA on day 6 (n ≥ 6). (G) *In vitro* MFE activity assay showing juvenile hormone III production from methyl farnesoate in the presence of NADPH. Heat-inactivated enzyme extracts and substrate-only blanks were included as negative controls to verify enzymatic specificity and catalytic activity (n ≥5). (H) Cumulative percentage of honeybees initiating out-hive activity from day 0 to day 15 (n = 32). (I) Schematic illustration of DWV infection enhances PPP activity and NADPH production in the honeybee brain, thereby promoting MFE-mediated JH biosynthesis and accelerating worker behavioral maturation. Control bees were injected with PBS, and DWV-treated bees were injected with 1×10^4 viral copies per bee. Data in panel (D) were normalized to day 2, whereas all other relative data were normalized to the control group at the corresponding time point. Data are presented as mean ± SD. Statistical analyses were performed using Student's t-test, one-way ANOVA, or two-way ANOVA, as appropriate. Asterisks indicate significant differences (*P < 0.05, **P < 0.01, ***P < 0.001, ****P < 0.0001). Different letters indicate significant differences among treatment groups in panel (G). For the in

vitro MFE activity assay, crude enzyme extracts were incubated with methyl farnesoate under the indicated cofactor conditions, and juvenile hormone III production was quantified by ELISA.

Fig. 5

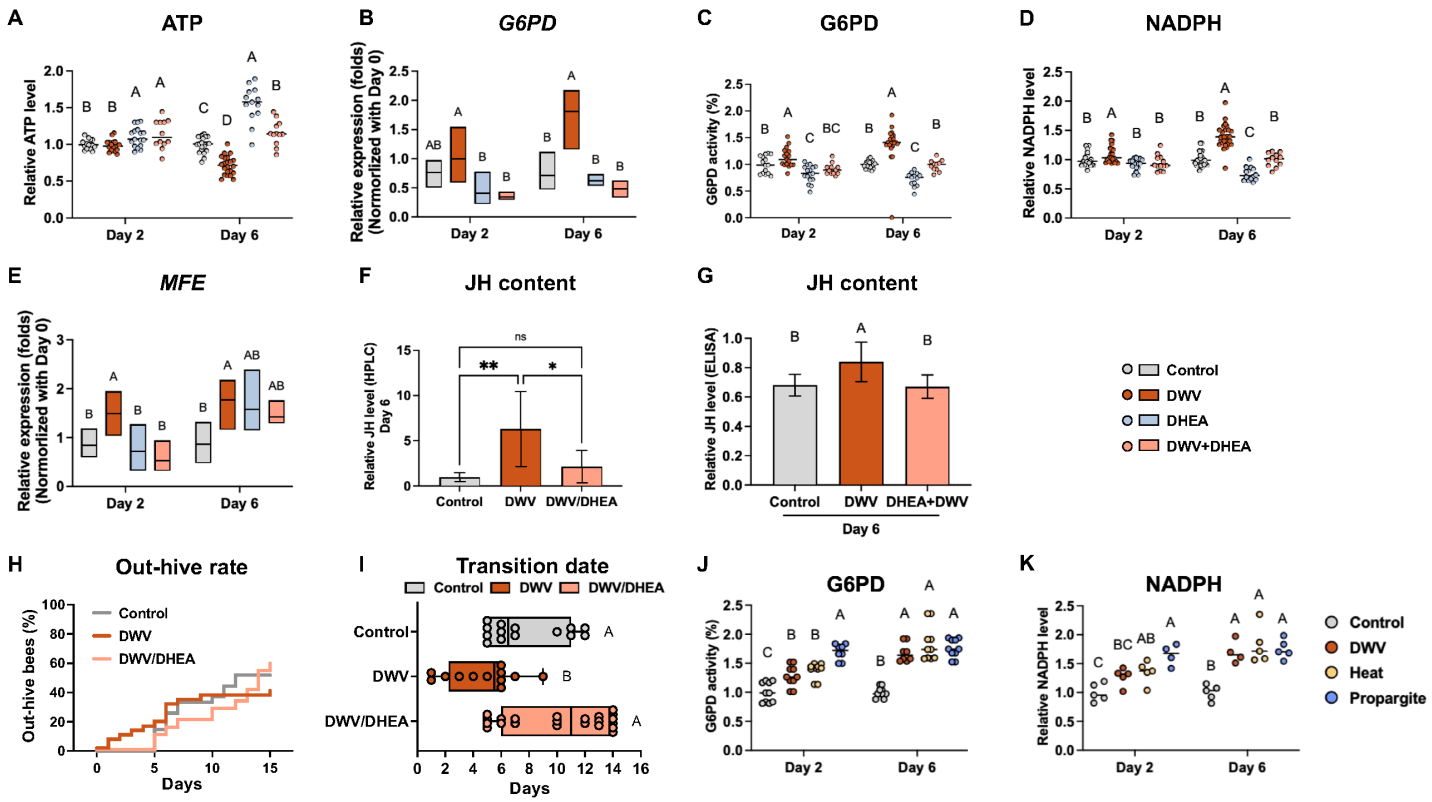


Figure 5

Functional perturbation of oxidative pentose phosphate pathway activity and enzymatic validation of NADPH-dependent juvenile hormone biosynthesis in DWV-infected honeybees. (A) Relative ATP levels in honeybee heads on day 2 and day 6 under control, DWV infection, DHEA treatment, and combined DWV+DHEA treatment (n ≥ 12). (B and C) Relative gene expression levels and enzymatic activity of *glucose-6-phosphate dehydrogenase* (G6PD) in honeybee heads on day 2 and day 6 under different treatments (n ≥ 4, n ≥ 11). (D) Relative NADPH levels in honeybee heads on day 2 and day 6 under different treatments (n ≥ 12). (E) Relative gene expression levels of *methyl farnesoate epoxidase* (*MFE*) in honey bee heads on day 2 and day 6 under different treatments (n ≥ 4). (F and G) Juvenile hormone (JH) levels in honeybee heads measured by HPLC (n ≥ 11) and ELISA (n ≥ 5) on day 6 under different treatments. (H) Cumulative percentage of honeybees initiating out-hive activity during the observation period in marked honeybees from day 0 to day 15 (n ≥ 32). Differences among treatments were assessed using the log-rank test. (I) The day of transition to out-hive activity in each treatment group (n ≥ 32). (J) Relative G6PD enzymatic activity in honeybee heads on day 2 and day 6 following viral, thermal (40°C), or pesticide (Propargite, 1/9000 dilution) treatments (n ≥ 8). (K) Relative NADPH levels in honeybee heads on day 2 and day 6 following the same treatments (n ≥ 4). Control bees were injected with PBS, and DWV-treated bees were injected with 1×10^4 viral copies per bee. Dehydroepiandrosterone (DHEA) was administered daily by feeding in 0.7 M sucrose solution at a final concentration of 2.5 μM.

Data in panel (B) and (E) were normalized to day 0, whereas all other relative data were normalized to the control group at the corresponding time point unless otherwise indicated. Data are presented as mean ± SD. Statistical analyses were performed using one-way ANOVA, two-way ANOVA, or log-rank test, as appropriate. Different letters indicate significant differences among treatment groups, and asterisks indicate significant differences (*P < 0.05, **P < 0.01, ***P < 0.001, ****P < 0.0001).

Fig. 6

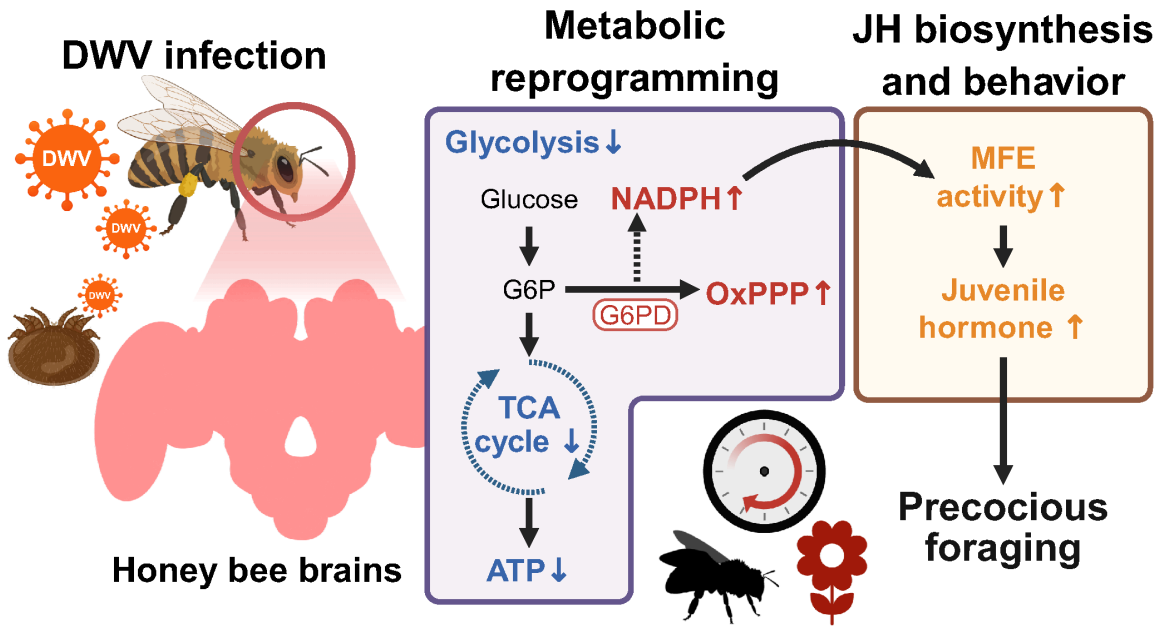


Figure 6

Proposed model of DWV-induced metabolic reprogramming linking oxidative pentose phosphate pathway activation to juvenile hormone biosynthesis in honeybees. Schematic illustration summarizing the proposed metabolic and endocrine regulation in DWV-infected honeybees. DWV infection alters glucose carbon allocation by reducing glycolytic flux and tricarboxylic acid (TCA) cycle activity while increasing pentose phosphate pathway (PPP) activity, leading to elevated NADPH production. Increased NADPH availability supports methyl farnesoate epoxidase-mediated juvenile hormone (JH) biosynthesis. Dietary supplementation with ribose and nicotinamide promotes NADPH production and further enhances JH biosynthesis. The model summarizes the relationship among glucose metabolism, redox regulation, and endocrine signaling in DWV-infected honeybees.

Supplementary Files

This is a list of supplementary files associated with this preprint. Click to download.

- Supplementary.docx